OPEN ACCESS

Ultrafast electron localization and screening in a transition metal dichalcogenide

Z. Schumacher[a], S. A. Sato[b,c] (ID), S. Neb[a] (ID), A. Niedermayr[a], L. Gallmann[a,1] (ID), A. Rubio[c,d] (ID), and U. Keller[a,1] (ID)

The coupling of light to electrical charge carriers in semiconductors is the foundation of many technological applications. Attosecond transient absorption spectroscopy measures simultaneously how excited electrons and the vacancies they leave behind dynamically react to the applied optical fields. In compound semiconductors, these dynamics can be probed via any of their atomic constituents with core-level transitions into valence and conduction band. Typically, the atomic species forming the compound contribute comparably to the relevant electronic properties of the material. One therefore expects to observe similar dynamics, irrespective of the choice of atomic species via which it is probed. Here, we show in the two-dimensional transition metal dichalcogenide semiconductor $MoSe_2$, that through a selenium-based core-level transition we observe charge carriers acting independently from each other, while when probed through molybdenum, the collective, many-body motion of the carriers dominates. Such unexpectedly contrasting behavior can be explained by a strong localization of electrons around molybdenum atoms following absorption of light, which modifies the local fields acting on the carriers. We show that similar behavior in elemental titanium metal [M. Volkov *et al.*, *Nat. Phys.* **15**, 1145–1149 (2019)] carries over to transition metal-containing compounds and is expected to play an essential role for a wide range of such materials. Knowledge of independent particle and collective response is essential for fully understanding these materials.

ultrafast dynamics | 2D materials | ultrafast spectroscopy | transition metal dichalcogenide | screening

Understanding ultrafast carrier dynamics driven by high-frequency electric fields is important for the engineering of materials toward applications in electronic and optoelectronic devices. Transition metal dichalcogenides (TMDCs) have sparked great interest in fundamental and applied science due to the abundance of observed physical phenomena (1, 2). Their unique electronic and mechanical properties, allowing to go from an indirect bandgap in bulk material to a direct bandgap by exfoliation to a monolayer, have contributed significantly to their popularity. Many effects, such as the strong exciton binding energy, the long exciton lifetime, and the spin selective valley dynamics have been studied extensively with optical and electronic probes. Combining different TMDC monolayers into new heterostructures has introduced further effects such as interlayer excitons and charge transfer (3–5) and trions in Moiré patterned potentials (6). Besides exfoliation techniques, which allow for precise control of the thickness and stacking of heterostructures, progress in chemical vapor deposition (CVD) has enabled the growth of large-area mono and few-layer samples (7). Some physics aspects, such as dark excitonic states (8), exciton generation time (9), and interlayer charge transfer (10, 11), are still actively researched due to the difficulty in characterizing such states. To date, most studies focus on the valley-, spin-, or layer-dependent properties, and only few studies have focused on the element-specific response of TMDCs (12–14).

Attosecond transient absorption spectroscopy (ATAS) allows for element and carrier-specific probe of excited states dynamics and has become a powerful tool to investigate electric field–driven carrier dynamics on the few femtosecond scale in semiconductors (15–19) and metals (20, 21), and strong field effects in dielectrics (22, 23). In most of these cases, ATAS uses a broadband extreme ultraviolet (XUV) pulse to probe the transition between core and excited states with attosecond or few-femtosecond temporal resolution. With the probe being resonant with a characteristic core level, ATAS becomes inherently element specific while its broad bandwidth simultaneously reveals the dynamics of both, pump-excited electrons and holes.

Here, we apply ATAS to a few-layer CVD-grown 2H $MoSe_2$ (6Carbon Inc.) with a bandgap of ≈1.55 eV. Surprisingly, we find qualitatively different dynamics in both conduction and valence band for probe transitions originating from either Mo or Se. This is remarkable because the band structure in the vicinity of the bandgap is formed by covalent

Significance

We study charge carrier dynamics following light absorption in the transition metal dichalcogenide semiconductor $MoSe_2$ with chemical element selectivity. Dynamics measured via the transition metal exhibit a many-body character with strong interactions between the carriers of the same type, while the dynamics probed via the chalcogen atoms indicate negligible interactions. These contrasting simultaneous observations are surprising because the atomic constituents of compound semiconductors typically contribute similarly to their relevant electronic properties. The different behaviors probed via the two atomic species result from strong charge localization around the transition metal atoms, which we find to be a universal phenomenon in materials containing this class of chemical elements. Knowing many-body and independent-particle contributions is essential for understanding carrier dynamics as a whole.

[1]To whom correspondence may be addressed. Email: gallmann@phys.ethz.ch or keller@phys.ethz.ch.

bonds between the *d*-orbitals from Mo and the *p*-orbitals from Se, with the two contributing to the density of states with similar magnitude. Such a qualitative difference in response was previously observed in the similar material MoTe$_2$ but not explained (12). In a recent publication, contrasting behavior observed for two W core-level transitions in WS$_2$ was suggested to originate from different degrees of localization of the initial states (24). In contrast, by combining our observed transient spectral features with ab initio calculations, we are able to attribute the qualitative difference to pump-induced real-space carrier localization into *d*-orbitals (i.e., final states) of the transition metal and the resulting local screening modification. Interestingly, the Se response remains entirely unaffected by such many-body dynamics. In MoSe$_2$, we find the localization effects to last longer than those in the elemental transition metal Ti and suggest that this faster decay is due to the much higher electron–electron scattering rates in the metal compared to a material with a bandgap.

Results

We simultaneously probe the core-level transitions from Mo 4*p* states and the spin-orbit split Se 3*d* states to the valence and conduction band (VB/CB) (Fig. 1). For multilayer MoSe$_2$, the maximum of the valence band is located at the Γ-point and has mostly 4*d*- and 4*p*-orbital contributions from Mo $d_{3z^2-r^2}$ and Se p_z orbitals, respectively. The orbital character of the conduction band minimum originates predominantly from d_{xy} and $d_{x^2-y^2}$ of Mo and p_x and p_y orbital contributions of Se. Furthermore, a nonnegligible $d_{3z^2-r^2}$ and p_z orbital contribution from Mo and Se atoms, respectively, is present in the conduction band (25–27). The strength of the *d*- and *p*-orbital contributions of the two respective atoms to the covalent bonds forming the band structure around

the bandgap is comparable as shown in our calculated projected density of states (Fig. 1C).

Our few-layer MoSe$_2$ sample was transferred onto a 30-nm-thin silicon nitride membrane as a substrate (Ted Pella) with excellent transparency in the energy window of our experiment. The broadband XUV probe spectrum from an attosecond pulse train spans photon energies from 30 to 70 eV. We use a 10-fs near-infrared (NIR) excitation pulse with a center photon energy of 1.54 eV and a peak intensity of $\approx 6 \cdot 10^{11}\,\mathrm{W/cm^2}$ at 1 kHz pulse repetition rate to promote carriers across the bandgap with a density of $\approx 2 \cdot 10^{21}\,/\mathrm{cm^3}$. At this field strength, we can neglect the magnetic field interaction because the dipole approximation is fully valid (28, 29). The relatively high pump-induced carrier density can be treated as an electron-hole liquid since it is above the Mott-transition (*SI Appendix*). The interferometric ATAS setup housed in vacuum is described in more detail elsewhere (30).

Spectral Response. The pump-induced transient changes in XUV absorption are shown in Fig. 2*A* as a function of time delay between the NIR pump and the broadband XUV probe pulse. Lineouts of that data integrated over a time span of ±20 fs for several time delays are plotted in Fig. 2*B*. The different core-level energies as shown in Fig. 1*B* allow us to separate the element-specific response with the probing photon energy. The Mo response covers the XUV photon energy range between 32 and 50 eV with the strongest signal for the Mo 4*p* core level to valence and conduction band (VB/ CB) transition (32 to 43 eV) and some weaker excitations into higher-lying and delocalized states above 47 eV. Of these, the 5*s* states contribute the most among the bound states (*SI Appendix*). The Se response for the XUV photon energy range of 54 to 60 eV shows two sharp alternating bands with increase and decrease in absorption that resemble the derivative of an absorption peak in
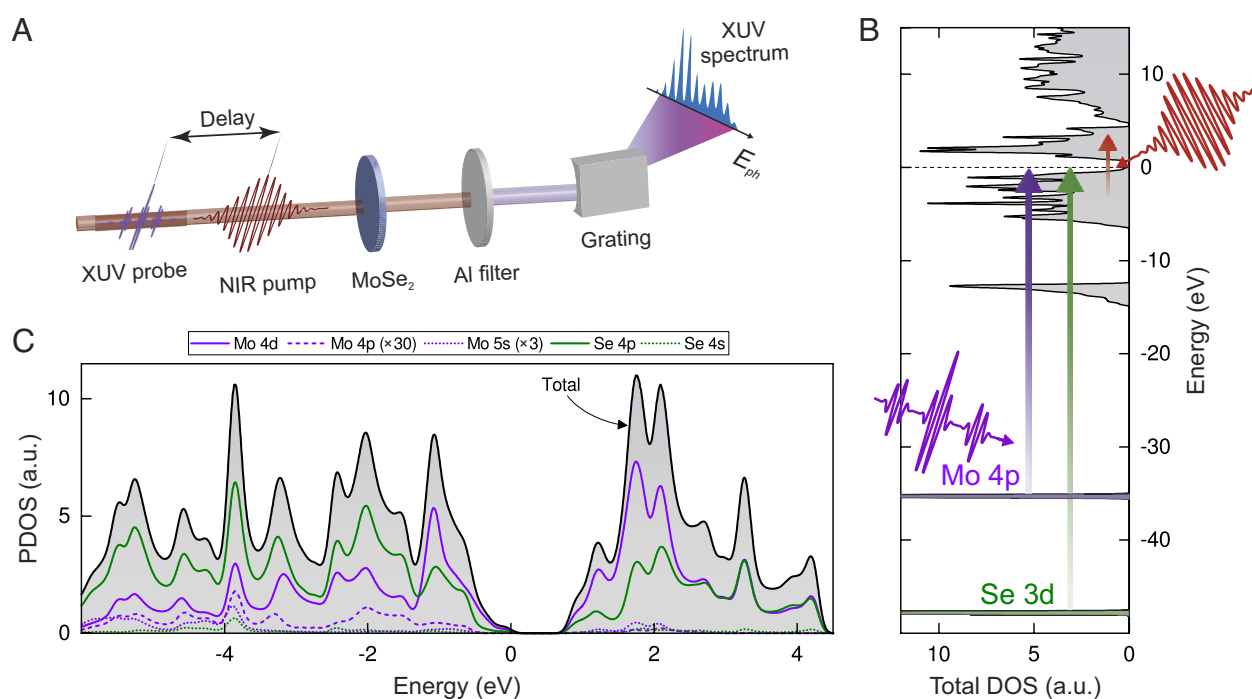

Fig. 1. (*A*) Experimental setup. A near-infrared (NIR) pump and XUV probe pulse are delayed in time. The residual NIR is eliminated by an aluminum filter before the transmitted XUV radiation is measured in a spectrometer. (*B*) Total density of states of bulk MoSe$_2$ calculated by density functional theory. The NIR pump excites carriers across the Fermi level, while the XUV probes the transitions from the Mo 4*p* and Se 3*d* core levels to the valence and conduction band (spin-orbit splitting of Se 3*d* not shown). We obtain an element-specific probe of the same final states via different core-level energies. (*C*) Projected density of states showing dominant contributions of Mo 4*d* (purple solid line) and Se 4*p* (green solid line) states to the valence and conduction bands. Mo 4*p* and Mo 5*s* have been multiplied by a factor for better visibility.
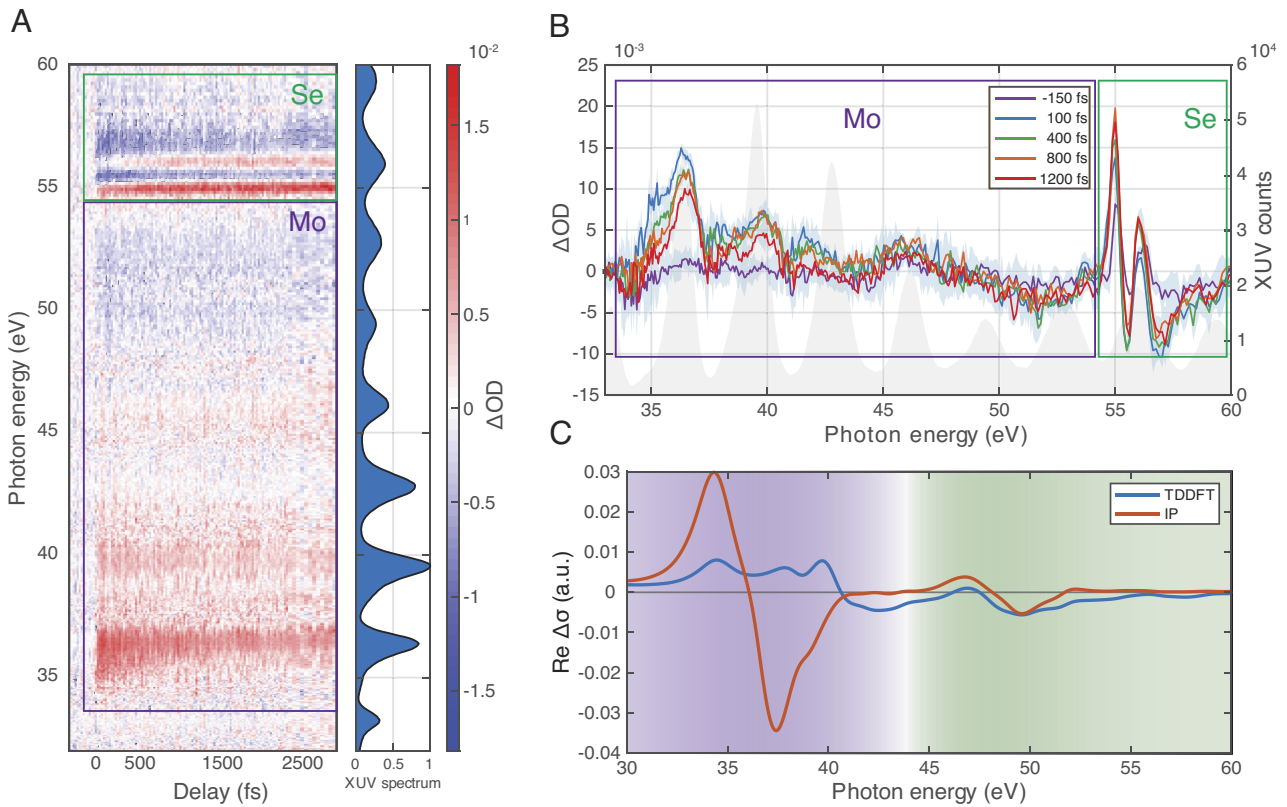
Fig. 2. (A) Attosecond transient absorption spectroscopy (ATAS) measurement of a few-layer MoSe$_2$ sample. The XUV response probed via the transitions from the Mo $4p$ states is enclosed by a purple frame, whereas the response probed via Se $3d$ states is marked by a green frame. This color code is maintained throughout this figure. (B) Profile of the induced change in optical density at different probe times (shaded areas represent the SD within the ±20 fs integration window). The transition metal Mo signal does not show any negative ΔOD around the bandgap, while the chalcogenide Se signal exhibits a clear negative ΔOD repeated by the $3d$ core-level spin orbit splitting. (C) Independent particle (IP) and TDDFT calculations show the change in the real part of the optical conductivity. The IP calculation features a negative response for the Mo transition. Only TDDFT calculations including many-body effects correctly reproduce the positive change for the Mo transition, thus highlighting the importance of localized screening due to electron localization into d-orbitals around the Mo atom after excitation. Spin-orbit splitting of the Se $3d$ core level is not considered in these calculations.

shape. The double appearance of this derivative-shaped feature arises from the spin-orbit split Se $3d_{3/2}$ and $3d_{1/2}$ transitions with an energy difference of ~1 eV (*SI Appendix*). In comparison, the Mo-specific signal in the VB/CB is more broadband and positive. As is shown below, this drastically contrasting behavior is not a probe-induced effect. Due to the mixed Mo d- and Se p-orbital nature of the VB/CBs accessed by the XUV probe pulse, such drastic difference in response is unexpected (Fig. 1C). Which of the two signatures reflect the actual VB/CB dynamics and how can we understand this apparent inconsistency taking into account well-known physics such as band filling, bandgap renormalization, and heating?

Discussion. The strongly energy-modulated, derivative-shaped features that appear in the Se response have been observed in previous ATAS measurements in semiconductors (see, e.g., refs. 12, 15, and 18). An NIR pump-induced increase of carriers in the conduction band manifests itself as a negative change of optical density (ΔOD) due to the reduced availability of unoccupied final states for the probe transition. The induced holes in the valence band lead to more available final states and an associated positive optical density change. The combination of these two effects leads to the derivative-shaped structure with sharp positive ΔOD in the valence band (missing electrons) and negative ΔOD in the conduction band (electrons excited from the valence band). This spectral response and associated dynamics can be well described by a simple model assuming a Gaussian distribution of carriers

in the conduction/valence band and the effects of band filling, bandgap renormalization, and (thermal) red shift (*SI Appendix*). A simple estimate based on carrier density of the induced bandgap renormalization results in ~160 meV renormalization (31, 32), even though higher values up to 500 meV have been reported for TMDCs (33–35). The described spectral response for the Se transition can be further confirmed with an independent particle model (IP) using time-dependent density functional theory (TDDFT) as shown in Fig. 2C (*SI Appendix*) (18).

The broad positive response in the Mo-specific absorption signal on the contrary does not indicate the increase in conduction band population which would be linked to a negative ΔOD. Only higher-lying bands >47 eV above the probed Mo core level show a broad negative response (Fig. 3C). The states in this energy region are a mix of higher-lying bound and delocalized states, with the Mo $5s$ contributing the most (*SI Appendix*).

The simple model based on band filling, bandgap renormalization, and heating-induced red shift that describes the signal observed for the Se probe transition completely fails to reproduce the measured spectral response for the Mo transition (see *SI Appendix* for more details). We therefore turn the focus to the different orbital configuration of the Mo and Se contributions in the VB/CB. Ab-initio calculations, in particular TDDFT with the adiabatic local density approximation (ALDA) and IP calculations (*SI Appendix*), are used to verify the origin of the difference in the spectral response (Fig. 2C). The TDDFT calculations can qualitatively reproduce the spectral shape for both initial probe states. It should be noted that
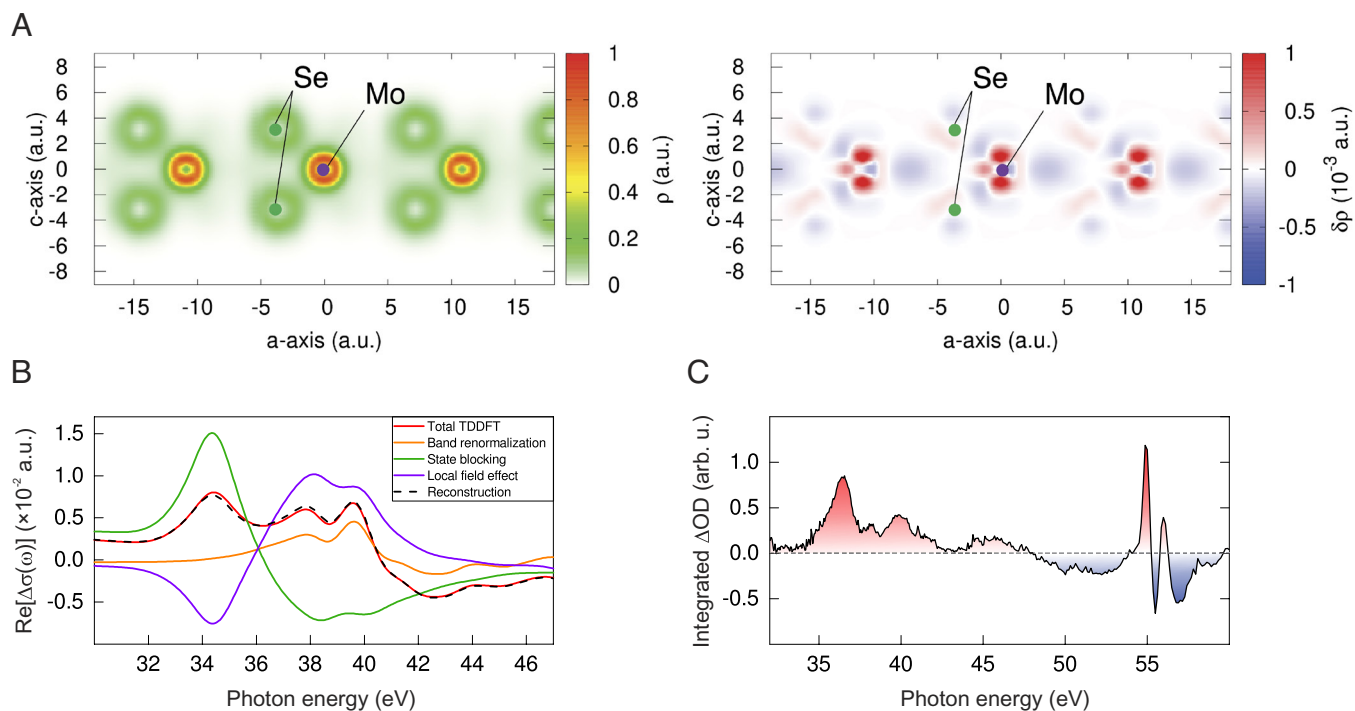
Fig. 3. (*A*) Real-space electron distribution and change induced by excitation with the NIR pump pulse. The electrons strongly localize around the Mo site within the *d*-orbital (positive changes in this figure indicate an increased electron density). The densities are evaluated for a thermalized electronic state, corresponding to delays of several tens of femtoseconds after excitation. (*B*) Decomposition of the TDDFT results in band filling, band renormalization, and local screening modification contributions. The *d*-orbital localization results in a screening response that compensates the band-filling effect and creates a broad overall positive change in absorption. (*C*) ATAS signal integrated over delay from 50 fs to 4.3 ps. A negative response is also seen for higher-lying states in the Mo signal at photon energies >47 eV which are dominated by Mo *5s* orbitals.

the calculated Se response is located at a different energy compared to the experiment. This is due to the different core-level energy of 45 eV instead of 55 eV found by TDDFT due to the lack of the core-hole effect in the ALDA. Furthermore, our TDDFT calculations do not consider spin-orbit splitting of the Se initial probe state. In contrast to the TDDFT, IP calculations do not include many-body effects, such as localized screening due to carrier localization. Fig. 2*C* shows the comparison between the TDDFT and IP calculations, where the Mo transition shows the most prominent difference, while the two models agree qualitatively for the Se case. The IP calculation for the Mo transition exhibits a prominent increase and decrease in the optical conductivity, the derivative-shaped structure mentioned above (see red line in Fig. 2*C*). This corresponds to an increased signal in the valence band at lower photon energy and to a decreased signal in the conduction band at higher photon energy. This is in contrast to the TDDFT calculation (blue line in Fig. 2*C*) with a broad positive response as seen also in the experiment (Fig. 2*B*). This difference between TDDFT and IP calculations indicates that the broad positive feature in the Mo response must be due to many-body effects.

To obtain further insights into the nature of these many-body effects, real space TDDFT calculations are performed to investigate the pump-induced charge redistribution. The results demonstrate a strong electron localization into the *d*-orbital around the Mo atom after the NIR pump pulse (Fig. 3*A*). A much weaker change with *p*-orbital symmetry is found around the Se atom. The *d*-orbital localization results in a strong local field effect with stronger screening as observed before in Ti metal (20). However, it comes as a surprise that this *d*-orbital localization is taking place in the TMDC semiconductors and leaves the chalcogen response unaffected even though the transition metal *d*-orbital and chalcogen *p*-orbital overlap defines the band structure in the VB/CB.

A decomposition of the TDDFT calculated change of absorption around the molybdenum transition in MoSe$_2$ highlights the quantitative contributions of band filling, renormalization, and local screening modification to the overall signal (Fig. 3*B*). A strong contribution of the local screening effect to the spectral response is found. Its spectral shape originates from the presence of the giant resonance in molybdenum that increases its energy separation from the probe initial state in response to the screening due to the localization into Mo 4*d* orbitals, resulting in a shape that counteracts the band filling signal.

Based on this theoretical analysis, we assign the origin of the measured broad spectral feature of the Mo transition to the valence electron localization occurring around the 4*d* orbital of molybdenum. The negative ΔOD response of the higher-lying bands probed by the Mo transition at photon energies between 47 and 54 eV shows further evidence for the screening effect most pronounced for *d*-orbitals (Fig. 3*C*). Remarkably, the Se response remains entirely unaffected by the electron localization, even though the conduction band is formed by an overlap of Mo 4*d* and Se 4*p* orbitals and the excited carrier population can be treated as an electron-hole liquid formed through global excitation from our NIR pump pulse (*SI Appendix*). The latter aspect renders the strong localization around the Mo sites a counter-intuitive observation.

Comparison with Ti and Dynamical Response. Similar strong localization into transition metal *d*-orbitals as for the Mo response in MoSe$_2$ and an associated broad positive change in absorption was first observed for Ti metal (20). In that study, it was shown that this is a universal feature for elementary *3d* transition metals and not present in more simple metals such as Al (21). Here, we find that the *d*-orbital localization still dictates the behavior of the
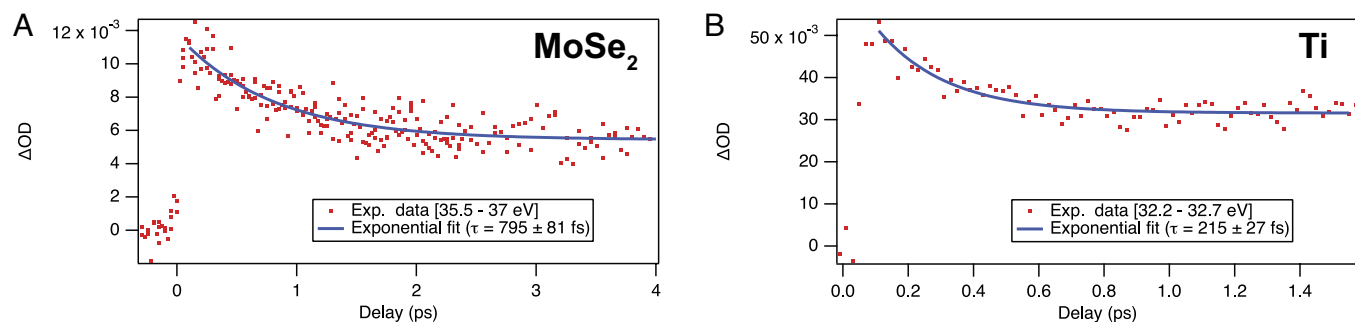
Fig. 4. (A) Decay of the main positive ΔOD signal in MoSe$_2$ in the photon energy band from 35.5 to 37 eV. An exponential fit reveals a decay time of ~800 fs while the overall signal remains positive for many picoseconds. (B) Decay of ΔOD signal in vicinity of giant resonance of Ti metal (see ref. 20 for details). The data have been integrated in a photon energy interval of 32.2 to 32.7 eV. An exponential fit yields a decay time of ~220 fs.

transition metal even when embedded into TMDC compounds. Furthermore, a recent control experiment in Al has shown that such localization does not occur in an ordinary (nontransition) metal (21). While the Se signal shows the typical ultrafast dynamics known from semiconductor materials, involving band filling, band renormalization, carrier thermalization, and thermal energy shifts (*SI Appendix*), the *d*-orbital localization dominating the Mo signal is a comparably long-lasting effect. The broad positive ΔOD feature in our ATAS data decays exponentially with a time constant on the order of 800 fs (Fig. 4*A*).

In Ti metal, on the contrary, the main positive feature around the Fermi energy decays within ~220 fs (Fig. 4*B*). In another dataset covering higher photon energies, we find 6 eV above the Fermi energy a negative ΔOD signal that appears about 75 fs after the pump pulse. While the latter Ti data have relatively poor statistics, a comparison with theory leads us to speculate that the appearance of the negative signal can be attributed to a fast decay of the *d*-orbital localization, revealing the state-filling part of the signal from the Ti *3d* and *4s* orbitals (see *SI Appendix* and ref. 20). Furthermore, we can assume that the electron localization in Ti decays much faster than the localization around Mo in the semiconductor MoSe$_2$ due to the much higher electron–electron scattering rates in the metal compared to a material with a bandgap.

Conclusion. We present the ultrafast measurement of excited-state carrier localization in semiconductors with transition metals such as MoSe$_2$. Through simultaneous element- and carrier-specific probing of the excited states, we identify the real-space carrier localization right after excitation around molybdenum. While the spectral response of the transition metal is dominated by screening effects with ultrafast *d*-orbital localization, the selenium is not affected by this collective response and can be described by an IP model with band filling, thermalization, and lattice heating. This can be considered surprising given that the NIR pump-excited carriers are well above the Mott-transition. This means the overall dynamics in such materials with transition metal elements cannot be described with an IP model. This may have implications for the applicability of the ubiquitous effective mass approximation for describing such semiconductors. The localization effects appear rapidly with the pump excitation on a few-femtosecond scale but appear to have a relatively long lifetime in semiconductors compared to the transition metal Ti. Furthermore, the real-space carrier localization adds an additional degree of freedom to the toolbox of engineering of opto-electronic materials, in addition to previously studied valley-selectivity and spin-momentum locking. Understanding the effects of the observed real-space carrier localization is the first step toward control of excited states

on an element-specific level in novel 2D energy materials. The qualitatively different ultrafast carrier dynamics observed for the transition metal Mo with the bonding *d*-orbitals and the chalcogen Se with the bonding *p*-orbitals forming both the conduction and valence bands demonstrate the need for element- and carrier-specific measurements also for heterostructure 2D systems where interlayer charge transfer occurs, a crucial process to advance TMDCs for future device applications. The present results are expected to be general and would be applicable to the whole family of homo and hetero TMD layered structures, including Moiré heterostructures.

Materials and Methods

Materials. The MoSe$_2$ samples are multilayer CVD-grown MoSe$_2$ films (6Carbon Technology), specified with a typical photoluminescence signal centered at 800 nm. The samples are provided on 30 nm-thick silicon nitride membranes from Agar Scientific (AGS171-1).

Laser Parameters. The pulse intensity is calculated based on the pulse width of 15 fs measured with spectral phase interferometry for direct electric-field reconstruction [SPIDER (36)] and a pulse energy of 1 µJ (1 mW average power at 1 kHz pulse repetition rate). The focal spot has dimensions of 80 µm (horizontal) by 60 µm (vertical). According to our spectral phase interferometry for direct electric-field reconstruction (SPIDER) measurements, 90% of the pulse energy is contained in the main pulse. Measurements of the spatial beam profile show that also 90% of the energy is focused into the central spot in the focal plane. We therefore estimate an intensity of $5.8 \cdot 10^{11}$ W/cm^2 ± $1 \cdot 10^{11}$ W/cm^2.

Delay Zero Calibration and Temporal Resolution. Delay zero calibration for the overlap between the NIR and XUV pulse train was obtained by acquiring a full RABBITT [reconstruction of attosecond beating by interference of two-photon transitions (37)] dataset in argon. The envelope of the side bands that appear in the region of pulse overlap is fitted to obtain delay zero and gain information about the cross-correlation width. The latter indicates a temporal resolution of our experiments of 10.3 ± 0.3 fs. From the oscillation period, we extract a center photon energy of our NIR pump pulse of 1.54 eV.

Data, Materials, and Software Availability. All data appearing in the main manuscript and SI can be found in the ETH research collection, doi: 10.3929/ethz-b-000604259 (38).

Author affiliations: [a]Department of Physics, ETH Zürich, 8093 Zürich, Switzerland; [b]Center for Computational Sciences, University of Tsukuba, Tsukuba, Ibaraki 305-8577, Japan; [c]Max Planck Institute for the Structure and Dynamics of Matter and Center for Free Electron Laser Science, 22761 Hamburg, Germany; and [d]Center for Computational Quantum Physics, Flatiron Institute, New York, NY 10010

Author contributions: Z.S., L.G., and U.K. designed the experiment; Z.S., S.N., and A.N. performed the experiment; S.A.S. and A.R. performed the theoretical calculations; Z.S., S.A.S., S.N., A.N., and L.G. analyzed data; and Z.S., S.A.S., L.G., A.R., and U.K. wrote the paper.

1. X. Yin *et al.*, Recent developments in 2D transition metal dichalcogenides: Phase transition and applications of the (quasi-)metallic phases. *Chem. Soc. Rev.* **50**, 10087–10115 (2021).
2. T. Chowdhury, E. C. Sadler, T. J. Kempa, Progress and prospects in transition-metal dichalcogenide research beyond 2D. *Chem. Rev.* **120**, 12563–12591 (2020).
3. C. Jin *et al.*, Identification of spin, valley and moiré quasi-angular momentum of interlayer excitons. *Nat. Phys.* **15**, 1140–1144 (2019).
4. H. C. Kamban, T. G. Pedersen, Interlayer excitons in van der Waals heterostructures: Binding energy, Stark shift, and field-induced dissociation. *Sci. Rep.* **10**, 5537 (2020).
5. J. Kunstmann *et al.*, Momentum-space indirect interlayer excitons in transition-metal dichalcogenide van der Waals heterostructures. *Nat. Phys.* **14**, 801–805 (2018).
6. E. Liu *et al.*, Signatures of moiré trions in $WSe_2/MoSe_2$ heterobilayers. *Nature* **594**, 46–50 (2021).
7. X. Wang *et al.*, Chemical vapor deposition growth of crystalline monolayer $MoSe_2$. *ACS Nano* **8**, 5125–5131 (2014).
8. J. Madéo *et al.*, Directly visualizing the momentum-forbidden dark excitons and their dynamics in atomically thin semiconductors. *Science* **370**, 1199–1204 (2020).
9. C. Trovatello *et al.*, The ultrafast onset of exciton formation in 2D semiconductors. *Nat. Commun.* **11**, 5277 (2020).
10. V. R. Policht *et al.*, Dissecting interlayer hole and electron transfer in transition metal dichalcogenide heterostructures via two-dimensional electronic spectroscopy. *Nano. Lett.* **21**, 4738–4743 (2021).
11. R. Wallauer *et al.*, Momentum-resolved observation of ultrafast interlayer charge transfer between the topmost layers of MoS_2. *Phys. Rev. B* **102**, 125417 (2020).
12. A. R. Attar *et al.*, Simultaneous observation of carrier-specific redistribution and coherent lattice dynamics in $2H$-$MoTe_2$ with femtosecond core-level spectroscopy. *ACS Nano.* **14**, 15829–15840 (2020).
13. A. Britz *et al.*, Carrier-specific dynamics in $2H$-$MoTe_2$ observed by femtosecond soft x-ray absorption spectroscopy using an x-ray free-electron laser. *Struct. Dyn.* **8**, 014501 (2021).
14. B. Buades *et al.*, Attosecond state-resolved carrier motion in quantum materials probed by soft x-ray XANES. *Appl. Phys. Rev.* **8**, 011408 (2021).
15. F. Schlaepfer *et al.*, Attosecond optical-field-enhanced carrier injection into the GaAs conduction band. *Nat. Phys.* **14**, 560–564 (2018).
16. M. Schultze *et al.*, Attosecond band-gap dynamics in silicon. *Science* **346**, 1348 (2014).
17. H. Mashiko, K. Oguri, T. Yamaguchi, A. Suda, H. Gotoh, Petahertz optical drive with wide-bandgap semiconductor. *Nat. Phys.* **12**, 741–745 (2016).
18. M. Zürch *et al.*, Direct and simultaneous observation of ultrafast electron and hole dynamics in germanium. *Nat. Commun.* **8**, 15734 (2017).
19. M. Zürch *et al.*, Ultrafast carrier thermalization and trapping in silicon-germanium alloy probed by extreme ultraviolet transient absorption spectroscopy. *Struct. Dyn.* **4**, 044029 (2017).
20. M. Volkov *et al.*, Attosecond screening dynamics mediated by electron localization in transition metals. *Nat. Phys.* **15**, 1145–1149 (2019).
21. A. Niedermayr *et al.*, Few-femtosecond dynamics of free-free opacity in optically heated metals. *Phys. Rev. X* **12**, 021045 (2022).
22. M. Lucchini *et al.*, Attosecond dynamical Franz-Keldysh effect in polycrystalline diamond. *Science* **353**, 916–919 (2016).
23. M. Schultze *et al.*, Controlling dielectrics with the electric field of light. *Nature* **493**, 75–78 (2013).
24. H.-T. Chang *et al.*, Coupled valence carrier and core-exciton dynamics in WS_2 probed by few-femtosecond extreme ultraviolet transient absorption spectroscopy. *Phys. Rev. B* **104**, 064309 (2021).
25. R. Roldán, F. Guinea, "Electronic properties and strain engineering in semiconducting transition metal dichalcogenides" in *2D Materials: Properties and Devices*, P. Avouris, T. Low, T. F. Heinz, Eds. (Cambridge University Press, Cambridge, 2017), chap. 14, pp. 259–278, 10.1017/9781316681619.015.
26. G.-B. Liu, W.-Y. Shan, Y. Yao, W. Yao, D. Xiao, Three-band tight-binding model for monolayers of group-VIB transition metal dichalcogenides. *Phys. Rev. B* **88**, 085433 (2013).
27. J. Silva-Guillén, P. San-Jose, R. Roldán, Electronic band structure of transition metal dichalcogenides from Ab initio and slater-koster tight-binding model. *App. Sci.* **6**, 284 (2016).
28. J. Maurer, U. Keller, Ionization in intense laser fields beyond the electric dipole approximation: Concepts, methods, achievements and future directions. *J. Phys. B At. Mol. Opt. Phys.* **54**, 094001 (2021).
29. A. Ludwig *et al.*, Breakdown of the dipole approximation in strong-field ionization. *Phys. Rev. Lett.* **113**, 243001 (2014).
30. R. Locher *et al.*, Versatile attosecond beamline in a two-foci configuration for simultaneous time-resolved measurements. *Rev. Sci. Instrum.* **85**, 013113 (2014).
31. B. R. Bennett, R. A. Soref, J. A. D. Alamo, Carrier-induced change in refractive index of InP, GaAs and InGaAsP. *IEEE J. Quantum Electron.* **26**, 113–122 (1990).
32. P. A. Wolff, Theory of the band structure of very degenerate semiconductors. *Phys. Rev.* **126**, 405–412 (1962).
33. F. Liu, M. E. Ziffer, K. R. Hansen, J. Wang, X. Zhu, Direct Determination of band-gap renormalization in the photoexcited monolayer MoS_2. *Phys. Rev. Lett.* **122**, 246803 (2019).
34. A. Chernikov, C. Ruppert, H. M. Hill, A. F. Rigosi, T. F. Heinz, Population inversion and giant bandgap renormalization in atomically thin WS_2 layers. *Nat. Photonics* **9**, 466–470 (2015).
35. T. N. Lin *et al.*, Many-body effects in doped WS_2 monolayer quantum disks at room temperature. *npj 2D Mater. Appl.* **3**, 1–6 (2019).
36. C. Iaconis, I. A. Walmsley, Spectral phase interferometry for direct electric field reconstruction of ultrashort optical pulses. *Opt. Lett.* **23**, 792–794 (1998).
37. H. G. Muller, Reconstruction of attosecond harmonic beating by interference of two-photon transitions. *Appl. Phys. B* **74**, S17–S21 (2002).
38. Z. Schumacher *et al.*, Ultrafast electron localization and screening in a transition metal dichalcogenide. ETH research collection. https://www.doi.org/10.3929/ethz-b-000604259. 21 March 2023.